ACOUSTIC SCATTERING FROM SUBMERGED ELASTIC OBJECTS

ILKKA KARASALO[†] AND KURT OTTO[†]

Abstract. Numerical studies of hydroacoustic scattering from submerged 3D elastic bodies have been performed. The underlying applications are identification of objects buried in the seabed and design of embedding polymer bodies for fiber-optic hydrophones.

The first study concerns data from a sea trial for scattering from a buried concrete-filled tyre. We extend a previously reported analysis of the trial by using more realistic models of the tyre and the seabed. In the second study, we investigate the elastic wavefield inside a circular polymer disc immersed in water and excited by an incident plane wave. We compute the normal stress field inside the disc and the unit elongation of the polymer material along circular curves in the equatorial plane of the disc for some choices of polymer material.

For the buried tyre, the results provide an improved understanding of the trial data. The analysis indicates that the effects of seafloor roughness and sediment inhomogeneities on the data are smaller than previously believed, and that the tyre material is stiffer than homogeneous concrete, probably due to reinforcing steel bars. For the polymer disc, the results yield estimates of the sensitivity and bandwidth of hydrophones of the specified shape and material type.

Key words. scattering, boundary integral method, underwater acoustics, buried object, fiber-optic hydrophone

1. Introduction.

This report presents results from computational modelling of two different underwater acoustic applications encountered in the FOI research projects for Mine protection, Surveillance sonars, and Optical underwater sensors; (i) acoustic remote sensing for identification of objects buried in the seabed, and (ii) design of embedding polymer bodies for planar fiber-optic hydrophones. In both applications, the principal modelling task is to compute the acoustic field in a fluid medium containing a 3D body of elastic solid material.

We analyze the application scenarios by using numerical predictions based on full-field theory of acoustic fluid–solid interaction and scattering. In the remote sensing application, our purposes are to gain insight into the scattering contributions that make up the useful signal, and to investigate how well the numerical predictions in a well defined model scenario agree with experimental data from a sea trial. In the fiber-optic sensor application, we want to estimate the sensitivity and bandwidth of a proposed sensor design for some choices of polymer material.

A common, longer-term objective is to develop reliable software tools for modelling of acoustic scattering from objects submerged in shallow water or buried in the seabed. Pertinent applications for such tools include target signature prediction in systems for tactical sonar support or mine detection.

[†] Division of Systems Technology, Swedish Defence Research Agency, SE-172 90 Stockholm, Sweden (ilkka.karasalo@foi.se, kurt.otto@foi.se).

1.1. Identification of buried objects. In the first application, we analyze results from a sea trial for identification of buried objects using a ROV-mounted parametric sonar and bistatically located receivers. The trial was conducted at a shallow-water site in the Baltic Sea and was configured as shown in Fig. 1.1.

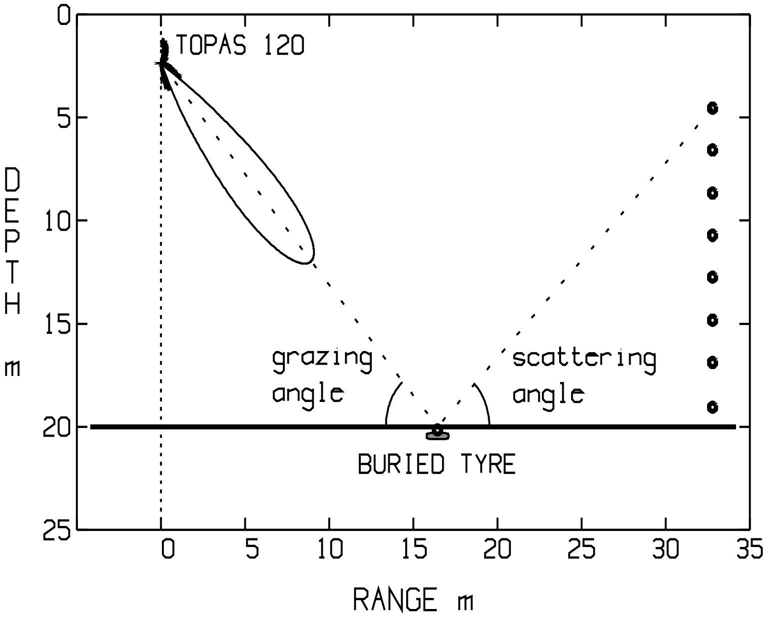

Fig. 1.1. *Identification of buried object: Experimental set-up.*

The seabed above the tyre was insonified by a ROV-mounted parametric transmitter, emitting Ricker-like pulses within a narrow lobe with oblique incidence angle. The center frequency of the pulses was 5 kHz, and the pulse repetition frequency 5 Hz. The scattered field was registered by an eight-hydrophone vertical array at 16 m range and by a single hydrophone on the seafloor above the tyre.

An initial analysis of results from the trial was reported in [5]. In this report, the analysis is extended towards more realistic models of the scattering body and the environment. The main extensions are to model the concrete as an elastic solid, and to use a two layered seabed model with a subbottom sediment layer interface at 0.8 m depth.

1.2. Fiber-optic hydrophone. As the second application, we study the dynamical response of a circular polymer disc immersed in water and excited by an incident plane acoustic wave. Such polymer discs are used for embedding the optical fiber of planar fiber-optic hydrophones [11]. The sensitivity of the hydrophone is proportional to the elongation of the embedded optical fiber, which is induced by the elastic wavefield in the polymer. A simple estimate of the fiber elongation is provided by the elongation of the polymer material along curves tracing the fiber core, but without the fiber present.

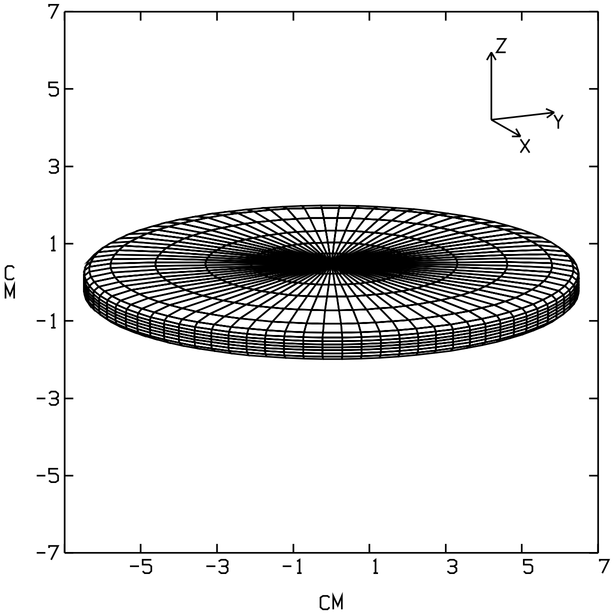

Fig. 1.2. *Model of a polymer disc with diameter* $d = 13$ cm *and thickness* $h = 1$ cm.

We have performed parametric studies of such discs for a number of different polymer materials, as characterized by their elastodynamic parameters. The discs have the shape shown in Fig. 1.2 with the intended fiber placed along a spiral in the equatorial plane of the disc. Our primary objective is to compute the average unit elongation of circles in the equatorial plane of the disc at operational frequencies of the hydrophone. A secondary objective is to extend the study of the wavefield inside polymer discs reported in [10] to a more realistic, i.e., elastic solid (instead of fluid) model of the polymer.

2. Summary of results.

2.1. Identification of buried objects. The agreement between the predicted and the observed traces at the topmost sensor of the vertical array is improved by the introduction of a subbottom layer interface in the seabed model. The late arrival observed in the data, but not in model predictions using a homogeneous seabed [5, Fig. 17], is predicted correctly both in amplitude and arrival time by a two-layer seabed model.

An important objective in buried object identification is to infer information of the internal structure of the object from observed data. As a simple illustration, we compare the observed traces at the topmost sensor of the vertical array with model predictions assuming the tyre material to be rigid, fluid, or elastic solid. Interestingly, the traces predicted by a fluid or a rigid structure are similar. They agree reasonably well with data, whereas those from the elastic solid structure show a significantly different echo shape. This perhaps surprising result indicates that the tyre material is in fact more stiff—with a higher shear velocity—than the homogeneous concrete assumed in the model.

A probable cause could be steel bars inserted inside the tyre for reinforcement of the concrete.

Furthermore, the agreement between the observed and the predicted distributions of acoustic energy among the hydrophones of the vertical array is improved significantly, cf. Figs. 4.7 and 4.8. This indicates that neglected contributions from seafloor roughness and sediment inhomogeneity to the observed data could be smaller than previously believed.

2.2. Fiber-optic hydrophone. We model the polymer disc as an elastic solid body, and study its dynamic excitation as a function of plane wave frequency and incidence angle for some choices of polymer material. At a constant frequency 2 kHz, the unit elongation of the polymer along circles tracing the intended fiber core is found to increase approximately linearly with Poisson ratio, see Fig. 5.6. Effects of resonances on the elongation appear at distinct frequencies, cf. Figs. 5.2–5.5. This might limit the operational bandwidth of the hydrophone. An important result from Sec. 5.3 is that the stress field excited in a disc of elastic solid material is significantly different from that predicted by a simplifying fluid model, which was anticipated in [10, p. 13].

3. Numerical method. Our numerical method is based on a frequency-domain boundary integral equation (BIE) formulation of scattering from a 3D body in a range-independent, optionally layered, fluid–solid medium. The BIE is solved numerically, and values of the single-frequency wavefield at specified points outside or inside the body are then computed using the integral representation. Transient fields are computed by Fourier synthesis of their single-frequency components. Details of the BIE formulation for impenetrable and shell-structured bodies are found in [7, 8, 9]. The BIEs for solid bodies and fluids are given in Appendix.

The numerical algorithms for assembling and solving the BIE are implemented in the XFEM-S code developed recently as part of the ISACS project. For the current state of the code, the following restrictions apply; (i) the medium must be range-independent, (ii) the scatterer must be strictly inside a fluid layer, (iii) the scatterer must have a smooth surface, (iv) the scatterer interior must be rigid, void, fluid, solid, or fluid enclosed by a thin elastic shell.

The model includes effects of waves penetrating into the body and multiple scattering at the body and at layer interfaces in the medium, but excludes effects of small-scale structural details within the scatterer, as well as small-scale inhomogeneities within the outside medium.

Except for low-frequency fields in simple media and simple scatterer geometries, the BIE approach is computationally demanding with workload and memory requirements increasing rapidly with frequency. However, the method is well suited for parallelization, and has been implemented [14] for parallel execution on networks of workstations under the MPICH message passing interface. In this way, computationally intensive broad-band scattering excitations like those in the buried object identification case can be handled.

4. Buried tyre. An initial analysis of the bistatic scattering trial illustrated in Fig. 1.1 was reported in [5]. In that analysis, the seabed was modelled as a homogeneous fluid halfspace, and the tyre as a fluid body. Although a good overall understanding of the trial results was achieved, it was found that more extensive modelling would be required to clarify some distinct unmodelled features of the data [5, Sec. 1.4].

In this section, we present results from such complementary analyses of the trial, using more realistic models of the seabed as well as the tyre. In particular, we include effects of subbottom layering and model the tyre as a solid body.

4.1. Model. In the computational model of the buried tyre trial, the field is excited by a vertical array of 63 point sources with aperture 9 m, weighted and steered to emit a beam with negligible side-lobes towards the seabed above the center of the tyre, cf. Fig. 1.1. The medium is composed of a homogeneous water halfspace above a two-layer fluid seabed. The tyre is shaped as a rotationally symmetric superellipsoid with surface

$$((x-x_0)^2+(y-y_0)^2)^2/a^4+(z-z_0)^4/c^4=1 \tag{4.1}$$

with half-axis lengths $a = 0.65$ m, $c = 0.15$ m. The top of the ellipsoid is 30 cm below the seafloor.

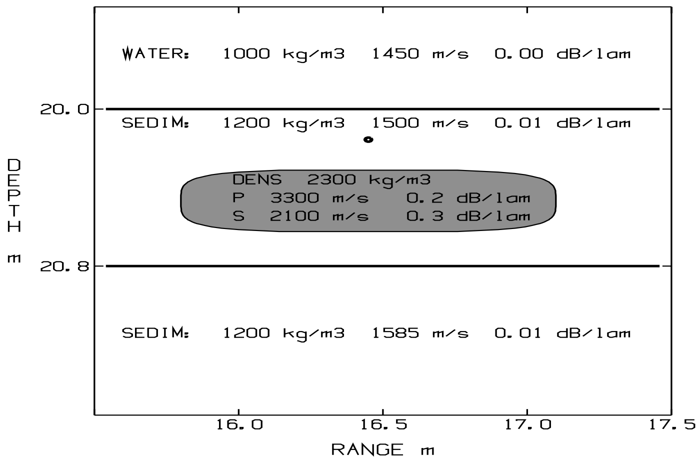

FIG. 4.1. *Buried tyre and enclosing medium.*

Figure 4.1 shows a close-up of the tyre, together with the acoustical parameters of the three fluid layers of the medium and the concrete material in the tyre. Note that the sensor originally deployed on the seafloor is assumed buried 15 cm into the sediment, in consistency with [5, Sec. 3, Fig. 10]. The thickness of the sediment layer in the model was chosen to 0.8 m guided by subbottom profiles from the 1997 ISACS trials [2, Ch. 4, Fig. 4.36]. The acoustic parameters of the two seabed layers were then obtained by a simple inversion procedure, to match the arrival time and amplitude of the observed late arrival at the top sensor of the vertical array, see Fig. 4.5 and [5, Fig. 17].

4.2. Pulse shape. Figure 4.2 shows the source waveform $s(t)$ used in the model simulations together with the average pulse $\bar{s}(t)$ recorded at calibration of the 5 kHz Ricker pulse from the TOPAS 120.

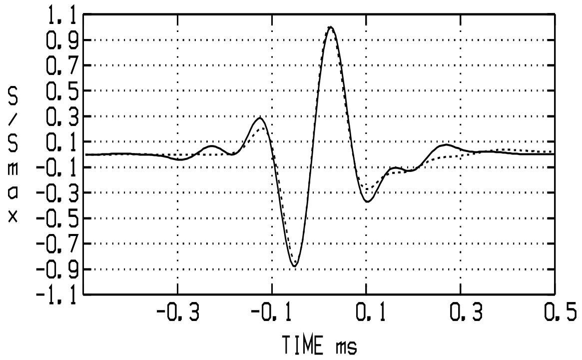

Fig. 4.2. *Model source waveform $s(t)$ (solid) and calibration data average $\bar{s}(t)$ (dashed).*

The theoretical Ricker pulse with center frequency f_c is

$$r(t) = -\frac{1}{2a}\frac{d^2}{dt^2}e^{-at^2}, \qquad \hat{r}(f) = 2(\pi^5/a^3)^{\frac{1}{2}}f^2e^{-\pi^2f^2/a}, \tag{4.2}$$

where $a = (\pi f_c)^2$. Since $\bar{s}(t)$ deviates significantly from $r(t)$, $s(t)$ was obtained by fitting a spline function to $\bar{s}(t)$ in a least squares sense, including penalty terms to suppress side-lobes in the time and the frequency domains, see [5, Sec. 2.3] for more details.

4.3. Seafloor sensor. By ray theory, the initial portion of the trace at the buried seafloor sensor is expected to be a sum of two arrivals along the ray paths shown in Fig. 4.3. For reference, the paths are denoted DI (source–seafloor–receiver) and S1 (source–seafloor–tyre–receiver), respectively.

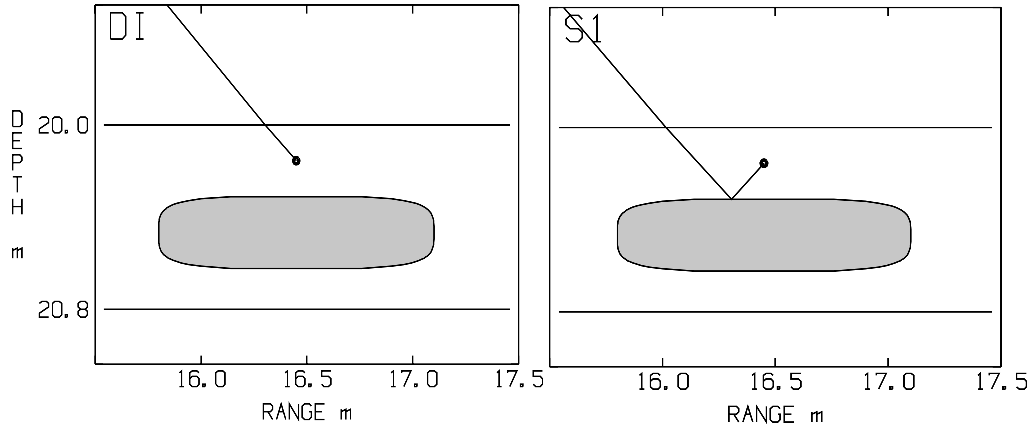

Fig. 4.3. *Ray paths corresponding to the two dominant initial arrivals at the buried seafloor sensor.*

Figure 4.4 shows the average experimentally observed trace at the seafloor sensor, together with the modelled trace. In the model, the sensor is assumed to have sunk 15 cm into the sediment, see Figs. 4.1 and 4.3.

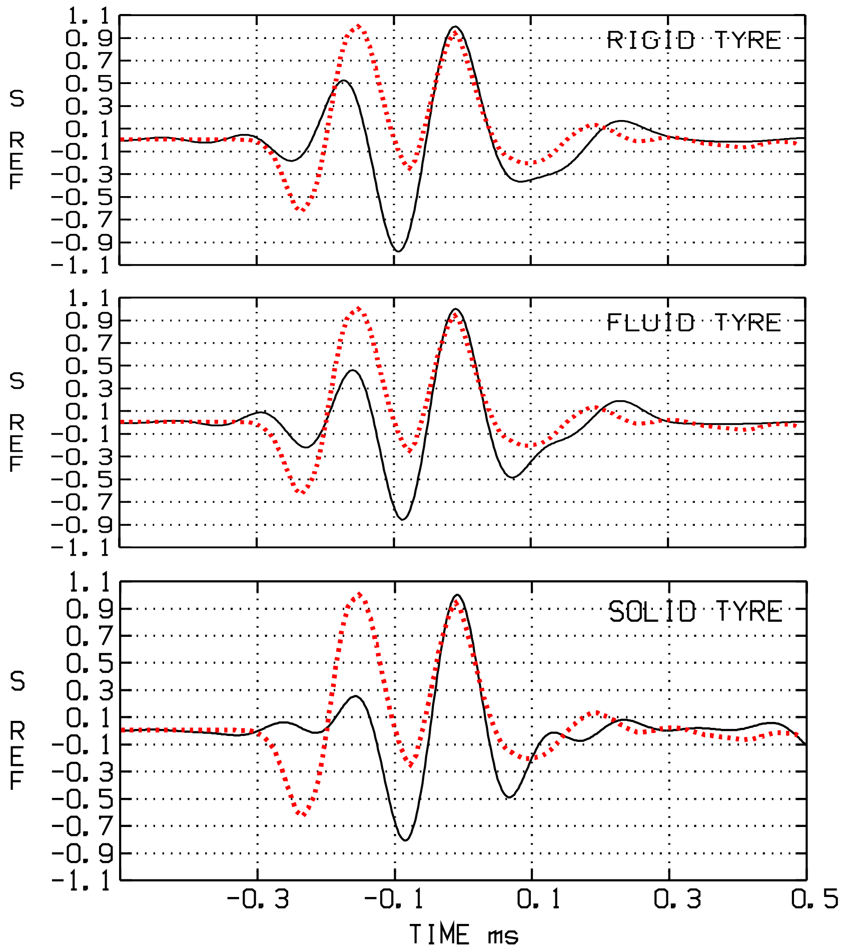

Fig. 4.4. *Normalized traces at the seafloor sensor. Solid: Predicted. Dotted: Average observed.*

The observed and modelled time differences between these two arrivals are in good agreement, as they should since the sensor-tyre distance in the model was obtained by the data matching procedure described in [5, Sec. 3.1]. The amplitudes of the modelled DI and S1 arrivals agree less well with data here than in [5, Fig. 11]. This could indicate, e.g., that the sensor was actually on the seafloor and the burial depth of the tyre was instead reduced by current-induced transport of the covering material. Alternatively, the sensor could be in a pothole developed in the loose material covering the tyre as a result of movements of the sensor and a marker cable attached to the tyre. We note that the predicted traces for the three types of tyre structure are similar in appearance, and that the mismatch of the relative amplitudes of the DI and the S1 arrivals is slightly worse for the solid tyre model than for the rigid and fluid models.

4.4. Top sensor of vertical array. The observed and the predicted traces at the top sensor of the verical array are shown in Fig. 4.5, using a rigid, a fluid, and an elastic solid model of the tyre.

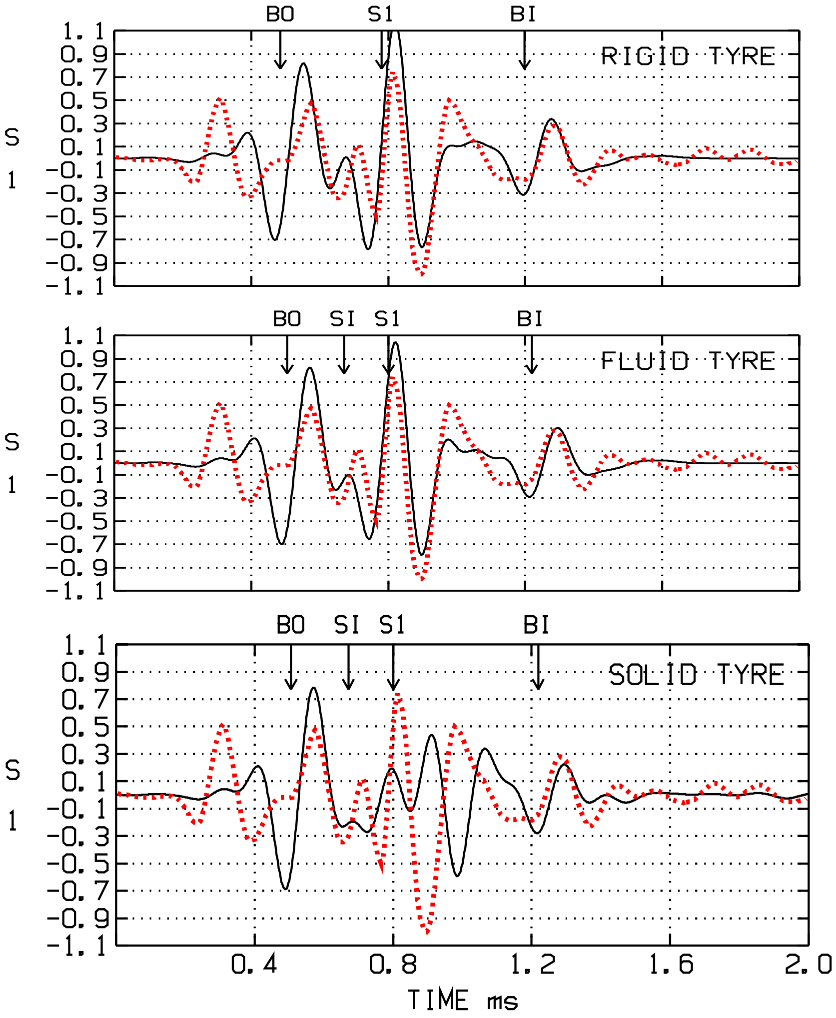

FIG. 4.5. *Normalized traces at the topmost sensor of the vertical array: Solid: Predicted. Dotted: Average observed.*

The downward-pointing arrows show arrival times along the ray paths from the source to the receivers displayed in Fig. 4.6. Note that the SI arrival represents sound that has penetrated through the tyre. Thus, the arrival time is not marked in the rigid (impenetrable) tyre diagram in Fig. 4.5. In fact, because of the large impedance contrast between the tyre and the sediment, the SI arrival is expected to be too weak to be visible in the data. Hence, the small peak at the SI arrival time $t \approx 0.65$ ms visible in all three frames is not the SI arrival but rather part of the interference pattern of the overlapping BO and S1 arrivals.

We note that, unlike [5, Sec. 3.2.1, Fig. 17], the BI arrival at $t \approx 1.3$ ms, i.e., sound reflected at the sediment layer interface 0.8 m below the seafloor, is predicted with good accuracy in both arrival time and amplitude for all three tyre models. The traces predicted by both the rigid tyre and the fluid tyre models are further in fairly good overall agreement with observed data, apart from the initial peak in the data at $t \approx 0.3$ ms. The cause of this peak is still uncertain, but it could be scattering from the top of an air-filled amplifier box adjacent to the seafloor sensor, or from a defective plastic buoy known to be left on the seafloor at the site. The polarity of this arrival appears in Fig. 4.5 to be opposite to that of the emitted pulse in Fig. 4.2, as it would for scattering from a low-impedance object such as an air-filled container.

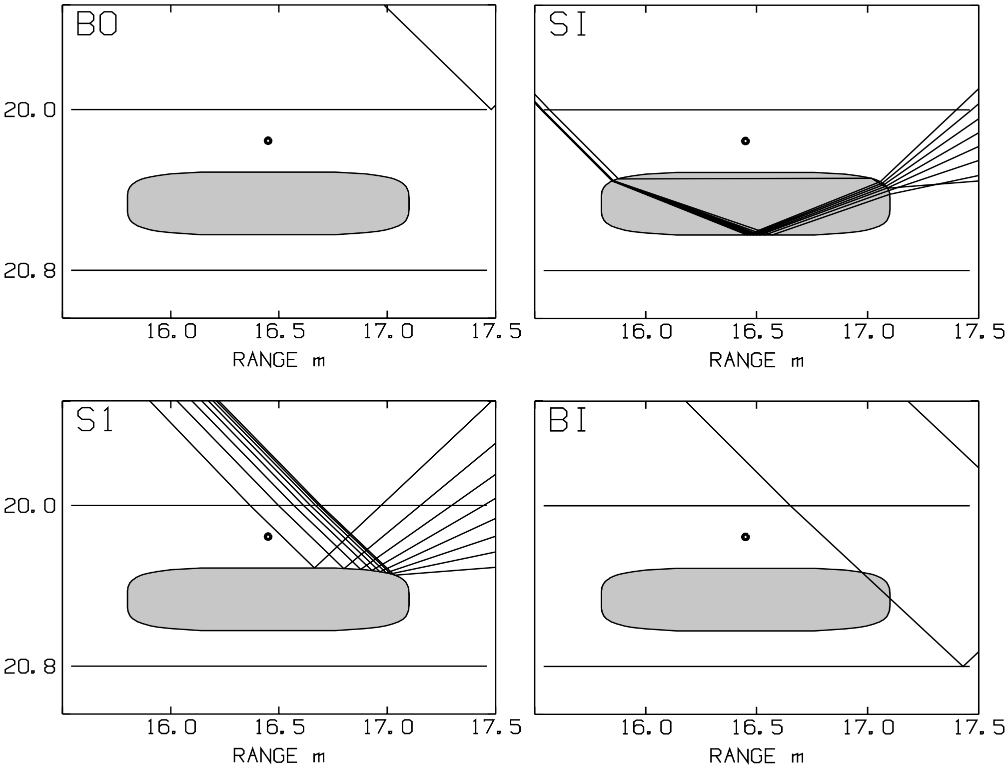

Fig. 4.6. *Ray paths from source to receivers in the vertical array.*

It is interesting to note that (i) the difference between the traces in Fig. 4.5 predicted by the rigid tyre and the fluid tyre models are small, and (ii) they agree significantly better with data than the trace from the elastic solid tyre model. This indicates that the tyre is in fact heavier and more rigid—in particular with a higher shear velocity—than homogeneous concrete with the parameters assumed in the model, see Fig. 4.1. A probable cause could be steel bars that were inserted inside the tyre for reinforcement of the concrete.

4.5. Spatial energy distribution. Figure 4.7 shows the sound energy received by the sensors of the vertical array as a function of sensor number. The energy values are defined as integrals of the squared signal values over 2 ms time-windows covering the dominant arrival section of each trace, as described in [5, Sec. 3.2.2, Fig. 19]. The values are normalized by the energy received by sensor 1 (the top sensor).

Each frame shows three energy distributions; the experimentally observed and those predicted by models with and without a tyre present in the seabed. The assumed structure of the model tyre is shown in the frames.

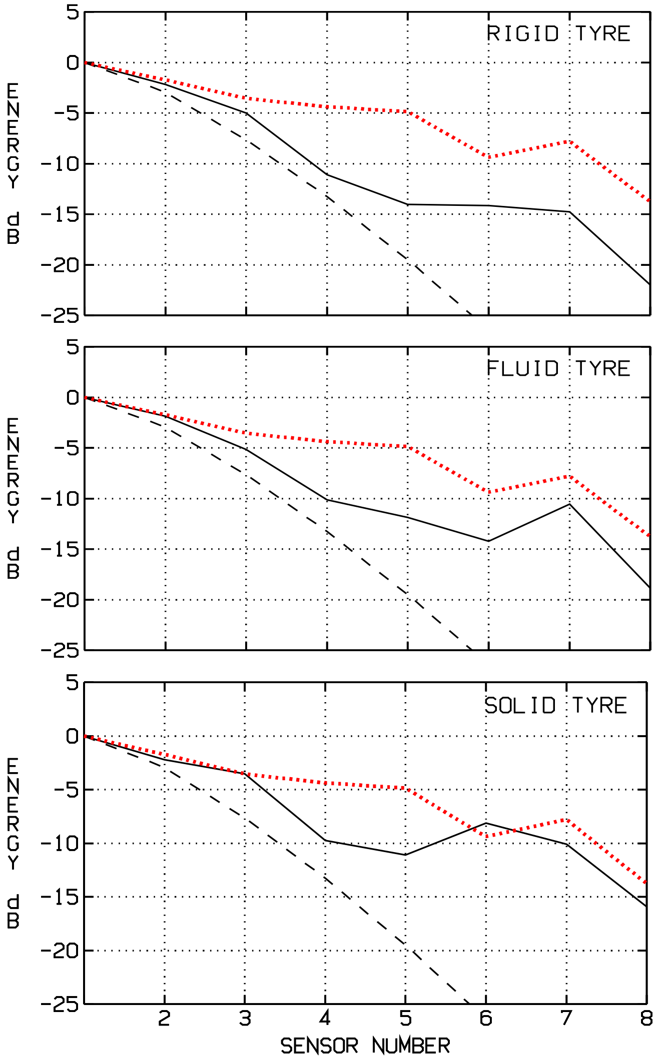

Fig. 4.7. *Energy received by the sensors of the vertical array: Solid: Modelled, layered seabed with tyre. Dashed: Modelled, layered seabed without tyre. Dotted: Observed.*

In all cases, the maximal energy occurs at sensor 1, which is closest to the specular scattering direction. With no scatterer in the seabed, energy decreases rapidly with sensor number, because of the narrow side-lobe free shape of the incident beam. A buried object with dimensions comparable with the footprint of the incident beam scatters a significant part of the sound in off-specular directions, resulting in a less concentrated energy distribution.

Figure 4.8 displays the fluid and solid tyre cases of Fig. 4.7, but with the seabed modelled as unlayered like in [5].

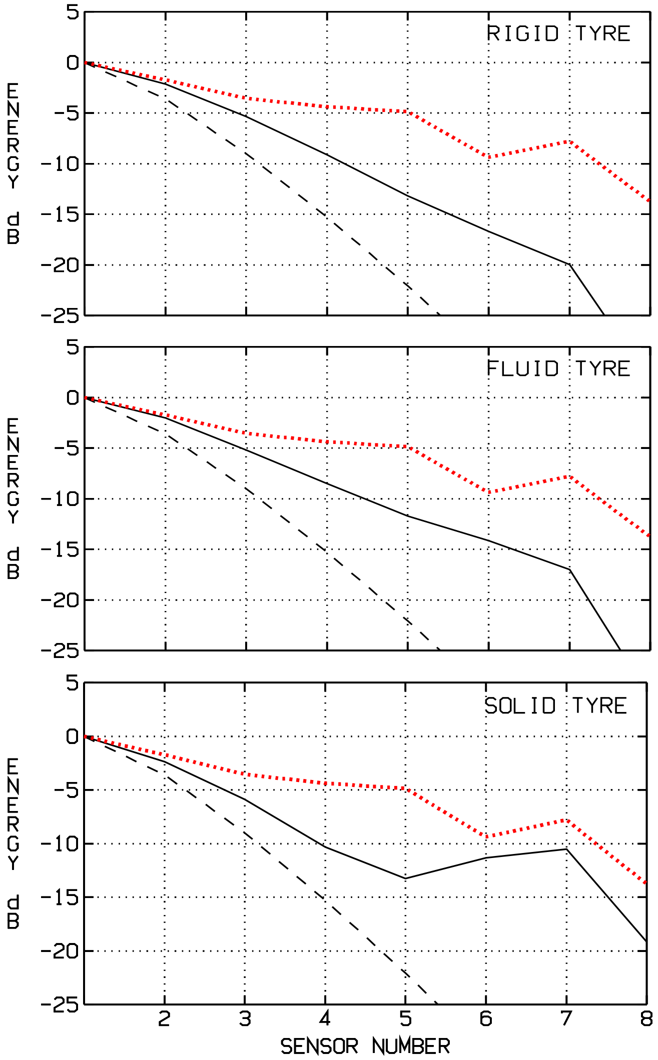

FIG. 4.8. *Energy received by the sensors of the vertical array: Solid: Modelled, unlayered seabed with tyre. Dashed: Modelled, unlayered seabed without tyre. Dotted: Observed.*

As seen from Figs. 4.7–4.8, both model extensions introduced in this study improve the fit of the predicted and observed energies significantly at sensors 6, 7, and 8.

As noted in the initial analysis [5, Sec. 3.2.2], the observed energy distribution is more uniform than that predicted by a fluid or rigid tyre and an unlayered seabed model, see also the top two frames of Fig. 4.8. In [5] this model–data discrepancy was attributed to effects of seafloor roughness and inhomogeneities within the sediment. An interesting result of the present study is that much of this feature in the data—including a local energy maximum at a sensor outside the reflected main beam—is in fact predicted by a medium model without roughness or inhomogeneities, see the last two frames of Fig. 4.7 and the last frame of Fig. 4.8. However, contributions from roughness and inhomogeneities may still be significant, as indicated by the remaining excess energy in the data, in particular at sensors 4 and 5.

5. Fiber-optic hydrophone. We use the same geometrical configuration for the polymer disc as in [10, Sec. 1]. Thus, the surface is approximated by

$$\frac{(x^2+y^2)^3}{a^6}+\frac{z^6}{c^6}=1.$$

This means that the surface is generated by rotating a superellipse, with semi-axes $a = 6.5$ cm and $c = 0.5$ cm, around the z-axis, see Fig. 1.2. The disc is excited by a plane wave defined as $\mathrm{Re}(p_{\mathrm{in}}(\boldsymbol{r})e^{-i2\pi ft})$,

$$p_{\mathrm{in}}(\boldsymbol{r}) = e^{i\boldsymbol{k}\cdot\boldsymbol{r}}, \quad \boldsymbol{k} = \boldsymbol{k}(\theta) = \frac{2\pi f}{c_{\mathrm{f}}}\big(\sin(\theta), 0, -\cos(\theta)\big) \tag{5.1}$$

with incidence angle θ and frequency f.

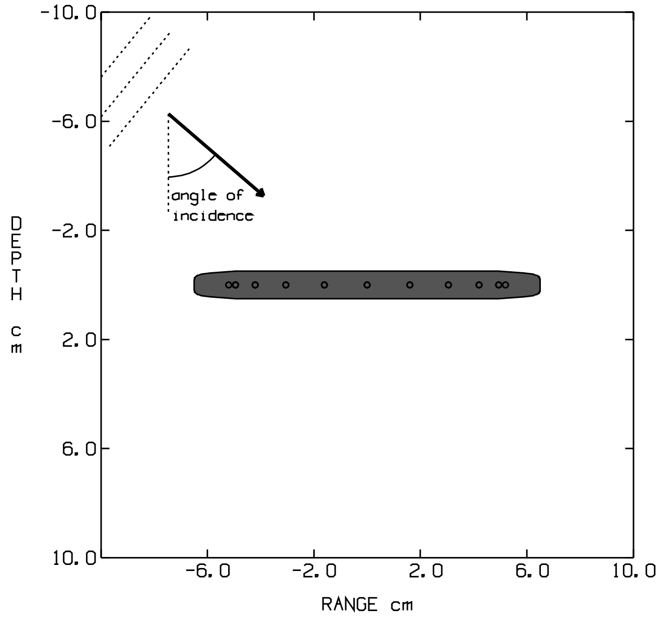

FIG. 5.1. *Model polymer disc and incident plane wave.*

The incident wave is propagating in a homogeneous water space with wave speed $c_{\mathrm{f}} = 1450$ m/s. The computational examples cover frequencies in the range 1 kHz $\leq f \leq$ 15 kHz.

5.1. Strain model. We are interested in computing the average unit elongation along a curve Γ tracing the fiber core, i.e.,

$$e_{\text{core}} \equiv L^{-1} \int_{\Gamma} \boldsymbol{t} \cdot \boldsymbol{\varepsilon}_{\text{core}} \cdot \boldsymbol{t} \, ds, \tag{5.2}$$

where $\boldsymbol{\varepsilon}_{\text{core}}$ is the strain tensor *for the fiber core*, $\boldsymbol{t}$ is the unit tangent vector of the curve, L is the arc length, and ds is the element of arc length. The fiber is wound in a tight spiral in the equatorial plane of the polymer body. We emulate one turn of such a spiral by letting Γ be a circle with radius r and center at the origin. Currently, we study the average unit elongation of the polymer material along the tracing curve Γ *without* the fiber present. That can be conceived as an approximation of (5.2) resulting in

$$e_{\text{core}} \approx e(r) = \frac{1}{2\pi r} \int_0^{2\pi} \widehat{\boldsymbol{\varphi}} \cdot \boldsymbol{\varepsilon} \cdot \widehat{\boldsymbol{\varphi}} \, r \, d\varphi = \frac{1}{2\pi r} \int_0^{2\pi} u_r(r, \varphi, 0) \, d\varphi, \tag{5.3}$$

where $\boldsymbol{\varepsilon}$ is the strain tensor, and u_r is the radial component of the displacement *for the polymer*. For azimuthally independent displacement fields, the *average* unit elongation $e(r)$ is the same as the unit elongation.

5.2. Unit elongation. We present examples that illustrate the unit elongation of the polymer material along concentric circles in the equatorial plane of the disc. The displacement field for the polymer has been computed numerically by the boundary integral method described in Section A.4. Subsequently, the unit elongation $e(r)$ is computed according to formula (5.3). The incidence angle θ is 0°, which leads to axially symmetric displacement fields. Various material parameters for the polymer has been utilized in the computations. We started by using the material parameters for polyurethane, just as in [10, Sec. 1]. The result is shown in Fig. 5.2.

For the computational results displayed in Figs. 5.3–5.6, the mass density was set to $\rho = 800$ kg/m^3 and the elasticity parameters varied.

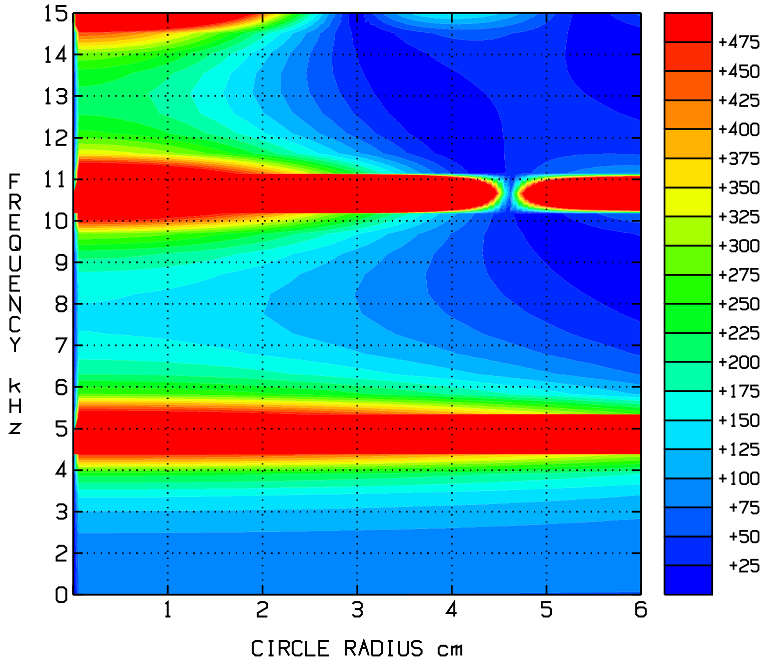

FIG. 5.2. *Unit elongation* $[10^{-12}]$ *of a tracing circle as a function of radius and frequency at incidence angle* $\theta = 0°$, *Poisson's ratio* $\nu = 0.45$, *Young's modulus* $Y = 0.85$ GPa.

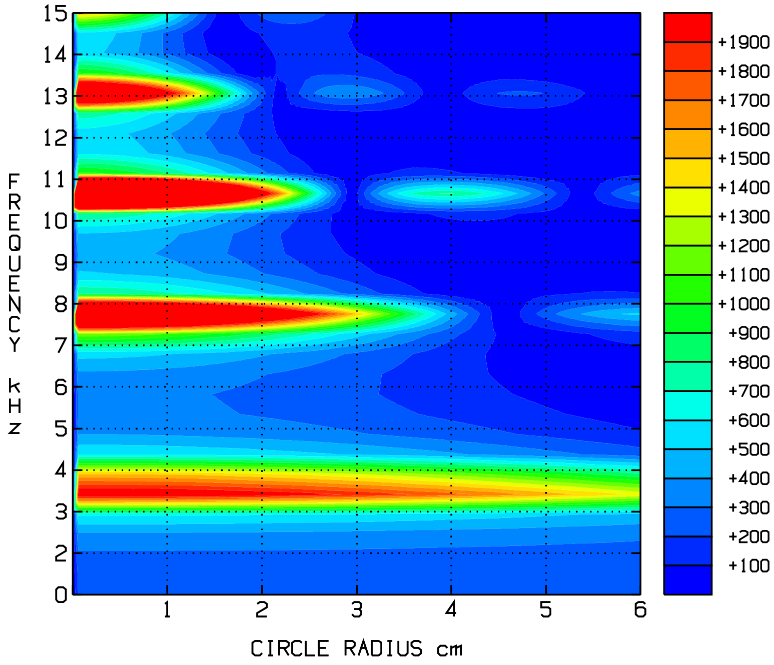

FIG. 5.3. *Unit elongation* $[10^{-12}]$ *of a tracing circle as a function of radius and frequency at incidence angle* $\theta = 0°$, *Poisson's ratio* $\nu = 0.45$, *Young's modulus* $Y = 0.30$ GPa *with loss tangent* 0.01.

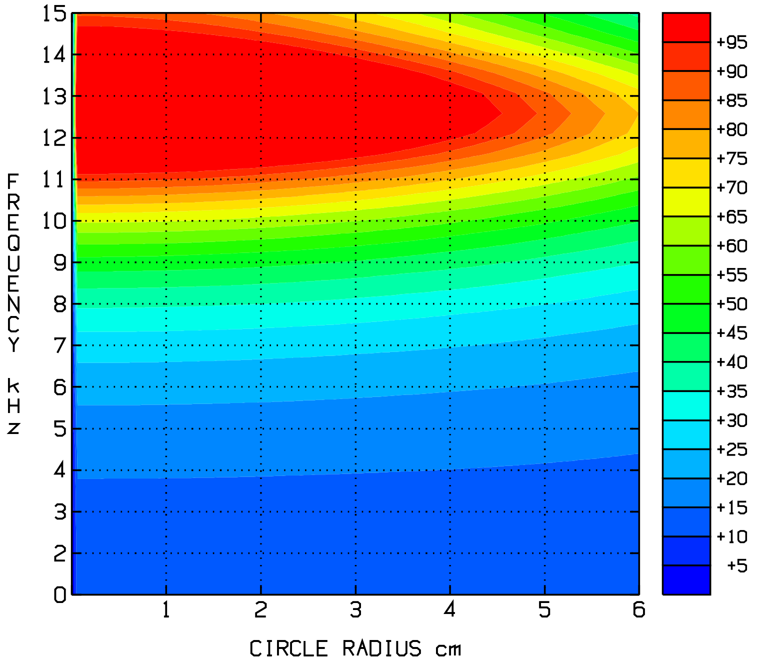

FIG. 5.4. *Unit elongation* $[10^{-12}]$ *of a tracing circle as a function of radius and frequency at incidence angle* $\theta = 0°$, *Poisson's ratio* $\nu = 0.45$, *Young's modulus* $Y = 5.0$ GPa *with loss tangent* 0.01.

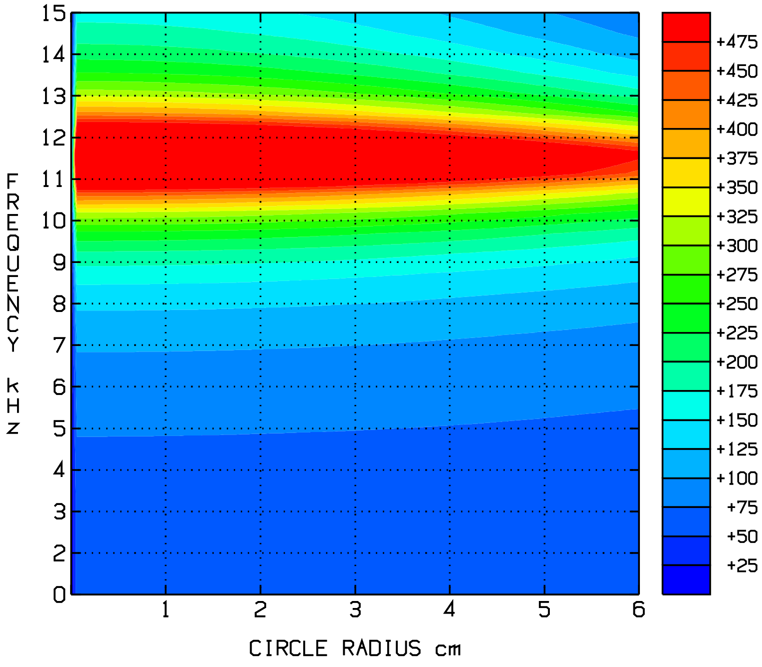

FIG. 5.5. *Unit elongation* $[10^{-12}]$ *of a tracing circle as a function of radius and frequency at incidence angle* $\theta = 0°$, *Poisson's ratio* $\nu = 0.25$, *Young's modulus* $Y = 5.0$ GPa *with loss tangent* 0.01.

Figures 5.2–5.5 show that the unit elongation is almost constant when the radius varies, but the frequency is fixed at any value less than roughly 5 kHz. This means that, in the low frequency range, there is no sharp optimum for where to put the fiber. For higher frequencies, there is a tendency that the unit elongation is larger for small circles. Hence, in the high frequency range, the best use of the fiber would be to place it close to the center of the disc. Similar observations have been made also for oblique incidence ($\theta > 0$). Fig. 5.6 displays the unit elongation at the fixed frequency $f = 2$ kHz. The unit elongation is clearly seen to be an increasing and approximately linear function of the Poisson ratio, at the chosen frequency.

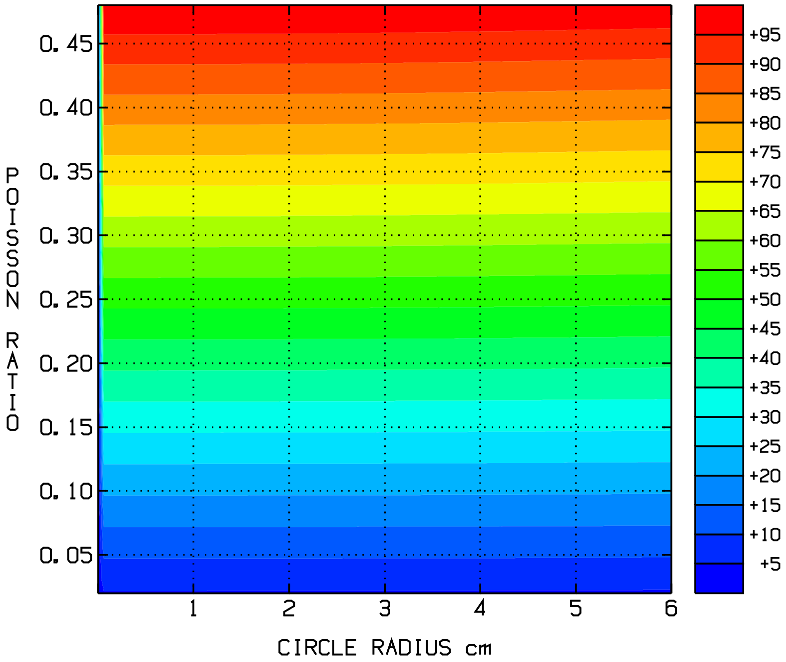

FIG. 5.6. *Unit elongation* $[10^{-12}]$ *of a tracing circle as a function of radius and Poisson ratio at incidence angle* $\theta = 0°$, *frequency* $f = 2$ kHz, *Young's modulus* $Y = 5.0$ GPa *with loss tangent* 0.01.

In Figs. 5.2–5.5 we observe that the unit elongation has maxima at certain frequencies. They are due to resonances—flexural vibration modes—of the disc. However, because of the symmetric shape and location of the circles, their elongation might not reveal all such resonance frequencies. A conclusive investigation of these resonances, using all the components of the strain field inside the disc, would be a straightforward task but could not be fitted into the time available. Another interesting extension of the present study would be to find optimal trajectories for the fiber, i.e., curves Γ along which the elongation e_{core} defined in (5.2) is maximal.

5.3. Stress. Here we present examples that illustrate the mean normal compressive stress field $-\frac{1}{3}\operatorname{tr}\big(\boldsymbol{\sigma}(\boldsymbol{r})\big)$ inside the polymer disc. Figure 5.7 shows the real part of $-\frac{1}{3}\operatorname{tr}\big(\boldsymbol{\sigma}(\boldsymbol{r})\big)$ inside the polymer disc for frequencies

$f = 1,\ 5,\ 10$ kHz at plane-wave incidence angle $\theta = 50°$. The points $\boldsymbol{r}$ cover an area obtained as the intersection of the xz plane and the polymer disc. Note that the vertical scale in Fig. 5.7 is expanded, distorting the apparent direction of propagation of the wave.

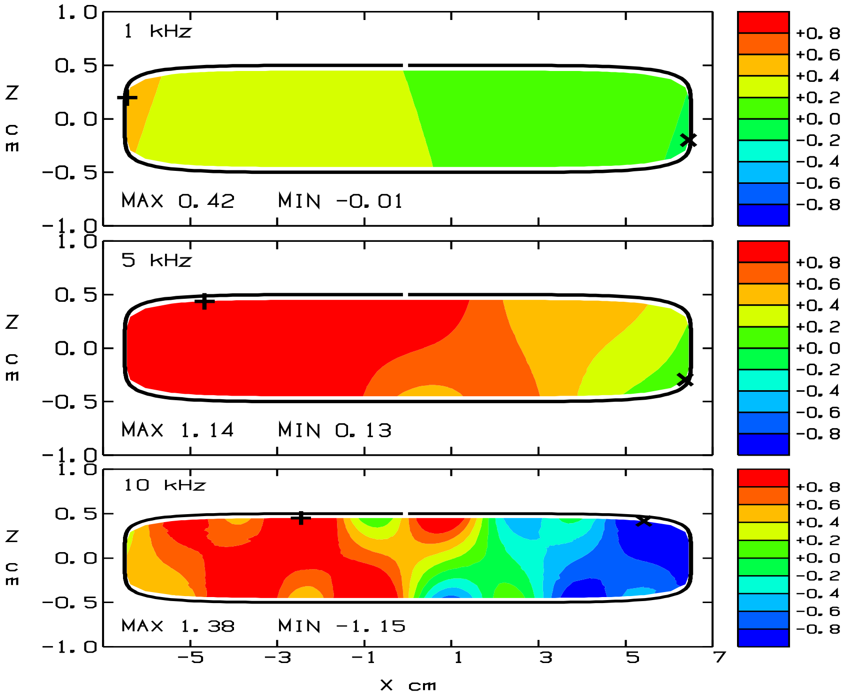

FIG. 5.7. *Real part of mean normal compressive stress inside the polymer disc at incidence angle* $\theta = 50°$.

For an inviscid fluid, the mean normal compressive stress is the same as the pressure. This means that [10, Fig. 4.2] shows the mean normal compressive stress in the simplifying case where the polymer was treated like a fluid. By comparing Fig. 5.7 and [10, Fig. 4.2], we see that the simplifying fluid model becomes less reliable when the frequency increases; even for the normal stress components.

Appendix. We now state the partial differential equations and integral equations that govern the strain and stress associated with acoustic scattering from an elastic body immersed in a fluid.

A.1. Fluid media. We consider time-harmonic sound waves in water. Transient acoustic fields would then be handled by Fourier synthesis. Neglecting sound absorption and assuming that the fluid is homogeneous, time-harmonic acoustic waves are governed by the Helmholtz equation

$$\nabla \cdot \nabla p + k^2 p = 0, \tag{A.1}$$

where $p(\boldsymbol{r})$ is the complex pressure, i.e., the scalar phasor [3, p. 337] of the acoustic pressure $\mathrm{Re}(p(\boldsymbol{r})e^{-i\omega t})$ [4, p. 73]. The wavenumber is given by $k = \omega/c_{\mathrm{f}} \equiv 2\pi f/c_{\mathrm{f}}$, where f is the frequency, and c_{f} is the sound speed.

A.2. Solid media. The scatterer is a linear isotropic elastic solid, which we assume is homogeneous. The time-harmonic elastic waves in such a medium are governed by the reduced Navier equations [1, p. 64]

$$\frac{\lambda+2\mu}{\rho}\nabla\nabla\cdot\boldsymbol{u}-\frac{\mu}{\rho}\nabla\times\nabla\times\boldsymbol{u}+\omega^2\boldsymbol{u}=0, \tag{A.2}$$

where $\boldsymbol{u}(\boldsymbol{r})$ is the vector phasor of the displacement $\operatorname{Re}(\boldsymbol{u}(\boldsymbol{r})e^{-i\omega t})$. The density is denoted by ρ, and the Lamé coefficients λ and μ (shear modulus) are related to Poisson's ratio ν and Young's modulus Y by

$$\lambda=\frac{\nu Y}{(1+\nu)(1-2\nu)}, \tag{A.3a}$$

$$\mu=\frac{Y}{2(1+\nu)}. \tag{A.3b}$$

The strain tensor $\boldsymbol{\varepsilon}$ is given by

$$\boldsymbol{\varepsilon}=\tfrac{1}{2}\big(\nabla\boldsymbol{u}+(\nabla\boldsymbol{u})^T\big).$$

It is related to the stress tensor $\boldsymbol{\sigma}$ by the linear constitutive equation

$$\boldsymbol{\sigma}=\lambda\operatorname{tr}(\boldsymbol{\varepsilon})\boldsymbol{I}+2\mu\boldsymbol{\varepsilon}, \tag{A.4}$$

where $\boldsymbol{I}$ is the identity tensor.

The Navier equations accommodate two main types of waves. The primary waves (P-waves) are irrotational ($\nabla\times\boldsymbol{u}=0$), and are also known as dilatation waves. The secondary waves (S-waves) are dilatation-free ($\nabla\cdot\boldsymbol{u}=0$), and are also known as shear waves. The wave speeds c_{p} and c_{s} for P-waves and S-waves, respectively, can be identified from (A.2), which combined with (A.3) yields

$$c_{\mathrm{p}}\equiv\sqrt{\frac{\lambda+2\mu}{\rho}}=\sqrt{\frac{1-\nu}{(1+\nu)(1-2\nu)}}\sqrt{\frac{Y}{\rho}}, \tag{A.5a}$$

$$c_{\mathrm{s}}\equiv\sqrt{\frac{\mu}{\rho}}=\sqrt{\frac{1}{2(1+\nu)}}\sqrt{\frac{Y}{\rho}}. \tag{A.5b}$$

A.3. Fluid–solid interaction. An accurate model for the acoustic response of the submerged scatterer entails solving (A.1) for the water and (A.2) for the elastic body, and coupling the solutions by appropriate interface conditions [13, p. 29]. For every point on the surface S of the body, the interface conditions on the stress (A.4) and on the displacement are given by

$$\boldsymbol{\tau}(\boldsymbol{u})\equiv\boldsymbol{\sigma}\cdot\boldsymbol{n}=-p\boldsymbol{n}, \tag{A.6a}$$

$$\boldsymbol{n}\cdot\boldsymbol{u}=(\rho_{\mathrm{f}}\omega^2)^{-1}\frac{\partial p}{\partial n}, \tag{A.6b}$$

where $\boldsymbol{n}$ is the outward unit normal of S, $\boldsymbol{\tau}$ is the surface traction, and ρ_{f} is the density of the fluid.

A.4. Boundary integral equations. There are several advantages [6] of using integral representations of the solutions to the three-dimensional Helmholtz equation (A.1) and Navier equations (A.2). For the solution $p(\boldsymbol{r}')$ at any point $\boldsymbol{r}'$ outside the surface S, an integral representation can be derived by employing Green's formula [12, p. 804], resulting in

$$p(\boldsymbol{r}') + \int_S \big(g(\boldsymbol{r},\boldsymbol{r}';k)\frac{\partial p}{\partial n} - \frac{\partial g}{\partial n}(\boldsymbol{r},\boldsymbol{r}';k)p\big)\,dS = p_{\text{in}}(\boldsymbol{r}'), \tag{A.7}$$

where $g(\boldsymbol{r},\boldsymbol{r}';k)$ is the free-space Green's function [12, p. 805] and p_{in} is a source term given by (5.1). Since the medium is homogeneous, the Green's function for the Helmholtz equation is known [12, p. 810] explicitly:

$$g(\boldsymbol{r},\boldsymbol{r}';k) = \frac{\exp(ik|\boldsymbol{r}-\boldsymbol{r}'|)}{4\pi|\boldsymbol{r}-\boldsymbol{r}'|}.$$

Thus, the solution outside the scatterer could be computed once the solution has been determined on the boundary S. An integral equation for the solution at the boundary is obtained from (A.7) in the limit $\boldsymbol{r}' \to \boldsymbol{r}' \in S$, yielding

$$\tfrac{1}{2}p(\boldsymbol{r}') + \int_S \big(g(\boldsymbol{r},\boldsymbol{r}';k)\frac{\partial p}{\partial n} - \frac{\partial g}{\partial n}(\boldsymbol{r},\boldsymbol{r}';k)p\big)\,dS = p_{\text{in}}(\boldsymbol{r}'). \tag{A.8}$$

The kernel in (A.7) exhibits an integrable singularity when $\boldsymbol{r}' \to \boldsymbol{r}' \in S$, cf. [13, Sec. 2.5.4]. Hence, special care must be taken in that limit.

The technique can be generalized to the elastic solid case, i.e., the Navier equations (A.2). An integral representation [13, p. 122] for the displacement field is

$$\boldsymbol{e}_\ell \cdot \boldsymbol{u}(\boldsymbol{r}') + \int_S \big(\boldsymbol{u}\cdot\boldsymbol{\tau}(\boldsymbol{G}\cdot\boldsymbol{e}_\ell) - \boldsymbol{\tau}(\boldsymbol{u})\cdot(\boldsymbol{G}\cdot\boldsymbol{e}_\ell)\big)\,dS = 0, \quad \ell = 1,2,3, \tag{A.9}$$

where $\boldsymbol{e}_\ell$ are unit vectors determining the directions of the point source. The symbol $\boldsymbol{G}$ denotes the Green's tensor, whose Cartesian components are

$$G_{ij} = (\rho\omega^2)^{-1}\big(k_{\text{s}}^2 g(\boldsymbol{r},\boldsymbol{r}';k_{\text{s}})\delta_{ij} + (g(\boldsymbol{r},\boldsymbol{r}';k_{\text{s}}) - g(\boldsymbol{r},\boldsymbol{r}';k_{\text{p}}))_{,ij}\big),$$

where k_{p} and k_{s} are the wavenumbers for P-waves and S-waves, respectively. Note that the Green's tensor is built entirely on Green's functions for the scalar Helmholtz equation. By taking the limit $\boldsymbol{r}' \to \boldsymbol{r}' \in S$ for (A.9), the following boundary integral equations are obtained:

$$\tfrac{1}{2}\boldsymbol{e}_\ell \cdot \boldsymbol{u}(\boldsymbol{r}') + \int_S \big(\boldsymbol{u}\cdot\boldsymbol{\tau}(\boldsymbol{G}\cdot\boldsymbol{e}_\ell) - \boldsymbol{\tau}(\boldsymbol{u})\cdot(\boldsymbol{G}\cdot\boldsymbol{e}_\ell)\big)\,dS = 0, \quad \ell = 1,2,3. \tag{A.10}$$

Equations (A.8) and (A.10) constitute a pressure–displacement formulation [13, p. 138] of boundary integral equations for scattering from an elastic body immersed in a fluid. The boundary integral equations are coupled by the interface conditions (A.6). Condition (A.6a) is enforced by replacing the surface traction $\boldsymbol{\tau}(\boldsymbol{u})$ in (A.10) with $-p\boldsymbol{n}$. By replacing $\frac{\partial p}{\partial n}$ in (A.8) with $\rho_{\text{f}}\omega^2\boldsymbol{n}\cdot\boldsymbol{u}$, condition (A.6b) is satisfied.

REFERENCES

[1] K. Aki and P. G. Richards, *Quantitative Seismology*, vol. I, W. H. Freeman and Company, New York, 1980.

[2] B. Berntsen, S. A. Frivik, and J. M. Hovem, eds., *ISACS Final Report*, Norwegian University of Science and Technology, Trondheim, Norway, 2000.

[3] D. K. Cheng, *Field and Wave Electromagnetics*, Addison–Wesley, Reading, MA, 2nd ed., 1989.

[4] F. B. Jensen, W. A. Kuperman, M. B. Porter, and H. Schmidt, *Computational Ocean Acoustics*, AIP Press, New York, 1994.

[5] I. Karasalo, *Model analysis of a bistatic scattering experiment*, Meth. Rep. FOA-R–00-01723-409–SE, Division of Systems Technology, Swedish Defence Research Agency, Stockholm, Sweden, 2000.

[6] I. Karasalo and J. Hovem, *Transient bistatic scattering from buried objects*, in Experimental Acoustic Inversion Methods for Exploration of the Shallow Water Environment, A. Caiti, J.-P. Hermand, S. M. Jesus, and M. B. Porter, eds., Kluwer Acad. Publ., Dordrecht, The Netherlands, 2000, pp. 161–176.

[7] I. Karasalo and J. Mattsson, *Numerical modelling of acoustic scattering by smooth inclusions in a layered fluid–solid medium*, in High Frequency Acoustics in Shallow Water, N. G. Pace, E. Pouliquen, O. Bergem, and A. P. Lyons, eds., NATO SACLANT, La Spezia, Italy, 1997, pp. 283–290.

[8] ———, *Accurate numerical modelling of scattering by 3D bodies and shells in a fluid–solid medium*, in Proc. Fourth European Conf. on Underwater Acoustics, A. Alippi and G. B. Cannelli, eds., vol. II, CNR-IDAC, Rome, Italy, 1998, pp. 691–696.

[9] ———, *Transient scattering from submerged objects—theoretical predictions and experimental results*, Tech. Rep. FOA-R–99-01169-409–SE, Division of Systems Technology, Swedish Defence Research Agency, Stockholm, Sweden, 1999.

[10] I. Karasalo and K. Otto, *A numerical study of the acoustic field in a fiber-optic hydrophone*, Meth. Rep. FOA-R–00-01780-409–SE, Division of Sensor Technology, Swedish Defence Research Agency, Linköping, Sweden, 2000.

[11] P. E. Martinsson, F. Kullander, and B. Knuthammar, *Construction and evaluation of a planar fiber-optic hydrophone for military applications*, Meth. Rep. FOA-R–00-01481-409–SE, Division of Sensor Technology, Swedish Defence Research Agency, Linköping, Sweden, 2000.

[12] P. M. Morse and H. Feshbach, *Methods of Theoretical Physics*, McGraw–Hill, New York, 1953.

[13] V. V. Varadan, A. Lakhtakia, and V. K. Varadan, eds., *Acoustic, Electromagnetic, and Elastic Wave Scattering*, vol. 1, Elsevier Science Publishers, Amsterdam, The Netherlands, 1991.

[14] T. Westerblom, *A parallel version of IS-Lab and the NFEM model for wave-propagation in range independent fluid–solid media*, Tech. Rep. FOA-R–98-00878-409–SE, Division of Systems Technology, Swedish Defence Research Agency, Stockholm, Sweden, 1998.